

See discussions, stats, and author profiles for this publication at: <https://www.researchgate.net/publication/280058665>

Propagation of Concentration Polarization Affecting Ions Transport in Branching Nanochannel Array

ARTICLE *in* ANALYTICAL CHEMISTRY · JULY 2015

Impact Factor: 5.64 · DOI: 10.1021/acs.analchem.5b01016 · Source: PubMed

CITATION

1

READS

29

5 AUTHORS, INCLUDING:



Chengyong Li

Guangdong Ocean University

23 PUBLICATIONS 135 CITATIONS

[SEE PROFILE](#)



Kang Wang

Nanjing University

54 PUBLICATIONS 1,202 CITATIONS

[SEE PROFILE](#)



Xing-Hua Xia

Nanjing University

224 PUBLICATIONS 8,589 CITATIONS

[SEE PROFILE](#)

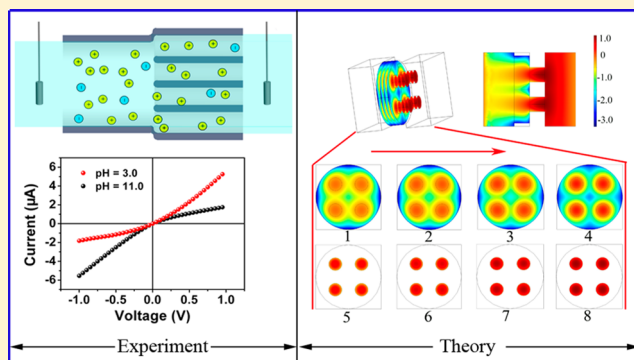
Propagation of Concentration Polarization Affecting Ions Transport in Branching Nanochannel Array

Cheng-Yong Li,[‡] Zeng-Qiang Wu,[‡] Chun-Ge Yuan, Kang Wang, and Xing-Hua Xia*

State Key Laboratory of Analytical Chemistry for Life Science and Collaborative Innovation Center of Chemistry for Life Sciences, School of Chemistry and Chemical Engineering, Nanjing University, Nanjing, Jiangsu 210093 China

Supporting Information

ABSTRACT: A new ionic current rectification device responsive to a broad range of pH stimuli has been fabricated using porous anodic alumina membrane with tailor-made branching nanochannel array. The asymmetric geometry is achieved by changing oxidation voltage using a simple two-step anodization process. Due to the protonation/deprotonation of the intrinsic hydroxyl groups upon solution pH variation, the nanochannels array-based device is able to regulate ionic current rectification properties. The ion rectification ratio of the device is mainly determined by the branching size and surface charges, which is also confirmed by theoretical simulations. In addition, theoretical simulations show that the slight difference in ion rectification ratio for the nanochannel devices with different branching numbers is due to the propagation of concentration polarization. Three dimensional simulations clearly show the nonuniform concentration profiles in stem nanochannel near the junction interface due to the presence of branching nanochannels. The present ionic device is promising for biosensing, molecular transport and separation, and drug delivery in confined environments.



Recently, the transport properties of electrolytes in nanoconfined spaces have attracted extensive interest due to the unique transport phenomena within spaces smaller than 100 nm at least in one dimension. For example, liquid flow through carbon nanotubes is found to be 4 to 5 orders of magnitude faster than that would be predicted from conventional fluid-flow theory.¹ This high fluid velocity is ascribed to the frictionless interface of the carbon nanotube wall. In the case of carbon nanotube, the surface is hydrophobic due to the extended benzene structure. When the surface of nanoconfined structures carries charges, the ion transport should show differences due to the electrostatic interactions. For example, ion transport in a 2 nm deep nanochannel is dominated by surface charges; i.e., the proton mobility increases by a factor of 4 over the bulk value at low concentration of electrolytes due to the serious overlap of the hydrogen-bonding network of the two hydration layers of the hydrophilic surfaces.² It has also been observed that the proton mobility will be enhanced even in nanochannels with one-dimensional size smaller than 330 nm although this is difficult to be understood.^{3,4} Recently, we found an anomalous non-Fickian transport behavior of polar molecule phenol in charged porous anodic alumina nanochannels.⁵ Our results showed that ion concentration, surface charge density, and nanochannel size play important roles in determining the diffusion flux. Due to these unique mass transport properties, nanopore and nanochannel promise potential applications in mimicking ion transport through biological membranes⁶ and in various separation techni-

ques,^{7–11} molecule delivery devices,^{1,2,5,12,13} sensing systems,^{14–21} and high efficacy electrochemical energy conversion systems.^{22–24}

The transport of charged species within asymmetric cone-shaped nanopores and nanopipettes exhibits specific behavior of ion current rectification (ICR) when the overlapping of electric double layer (EDL) becomes significant.²⁵ In ICR devices, anisotropic ion current dependent on voltage polarity occurs due to the presence of surface potential well within the nanodevices as in the semiconductor diodes. Such a non-biological rectifying phenomenon was observed in 1997 by Wei and Bard in a conically shaped quartz nanopipet.²⁶ Since then, various ICRs based on cylindrical,^{27–31} conical,^{32–42} double conical,⁴³ and cigar⁴⁴ nanopores and nanochannels have been proposed. However, all these devices are composed of a single nanopore or nanochannel with asymmetric geometry. Recently, ICR devices comprised of array nanochannels were developed by Zhai and co-workers, including light-gating heterogeneous nanochannels,⁴⁵ biomimetic funnel-shaped nanochannels,⁴⁶ and organic/inorganic hybrid nanochannels.⁴⁷ An ICR device based on branched nanochannels with tunable asymmetric geometry was also reported.⁴⁸ The transport of charged species in simply branched nanochannels was studied from experiments.

Received: March 8, 2015

Accepted: July 14, 2015

Published: July 14, 2015

In this work, we report the construction of an ICR device responsive to a broad range of pH stimuli using highly ordered porous anodic alumina (PAA) membrane with a tailor-made branching nanochannel array. Using traditional fabrication technologies, such as ion-track-etching technology,^{42,45,49,50} electron beam technology,^{51,52} and laser technology,^{26,40,53} films of single nanopore structure with precisely controlled size down to a few nanometers can be fabricated. However, these methods are complicated and require high cost and thus are inappropriate for large scale application. Especially, these technologies are not suitable for fabricating branching nanostructures. PAA membrane with a high density of parallel nanochannels can be successfully prepared using a simple two-step anodization method which is much easier and less expensive than the methods mentioned above. In addition, simulations with finite element method (FEM) have been used to describe the ICR mechanism of nanochannels with different size and surface charge density. Although the 2D theoretical simulations have been successfully applied to study the ionic rectification in single nanochannels,^{29,30,35,39} this model encounters difficulties in simulating branching structures due to the overlap of the electric field and concentration profile at the branching interface. Therefore, 3D FEM is used to study the ion rectification for reflecting the nature of ions transport in branching nanochannels. Simulation results show that propagation of enrichment and depletion zones of ions are critical for ICR in branching nanochannels. We believe that the present ICR device and the enlarged concentration polarization may find potential application in biosensing, molecular transport and separation, and drug delivery in confined environments.

RESULTS AND DISCUSSION

Fabrication and Characterizations of PAA Membranes with Branching Nanochannel Array. PAA membranes used in this work were prepared via a two-step aluminum oxidation process⁵⁴ (Figure S1, Supporting Information). Figure 1 shows the cross-sectional views of three different branching PAA membranes after chemical etching in a 5% phosphoric acid solution at 30 °C for 50 min. As reported, branching nanochannel can be created by reducing the anodizing voltage by a factor of $1/\sqrt{n}$ during the course of anodization.^{55–59} Funnel-structured PAA membrane (called nanochannel I) was fabricated by setting the oxidation voltage at 60 V for the second anodization process as in the first anodization process. The SEM image (Figure 1a) indicates that the interface longitudinally bridges two nanochannels with different sizes in the branches. The diameter of PAA nanochannel for the top (Figure S2a, Supporting Information) and bottom (Figure S2b, Supporting Information) is about 100 and 40 nm, respectively. The cross-sectional SEM image (Figure S2c, Supporting Information) clearly shows the significant contrast between the two layers with different nanochannel sizes. The darker area corresponds to the grown subnanochannels within preceding nanochannels. Both the thicknesses of two-tiered layers is estimated as ca. 45 μm . The geometry of the nanochannel structure in the membrane used here is further determined by characterizing the carbon nanotubes (CNTs) synthesized within the nanochannels (Supporting Information).⁶⁰ The high-magnification image of the CNTs interface (Figure 1b) clearly reveals the corresponding funnel geometry. The CNTs diameter is larger than the original nanochannel owing to thermal expansion of the template during growth.⁶¹ In Figure S2d, Supporting Information, a large bundle of CNTs collapse

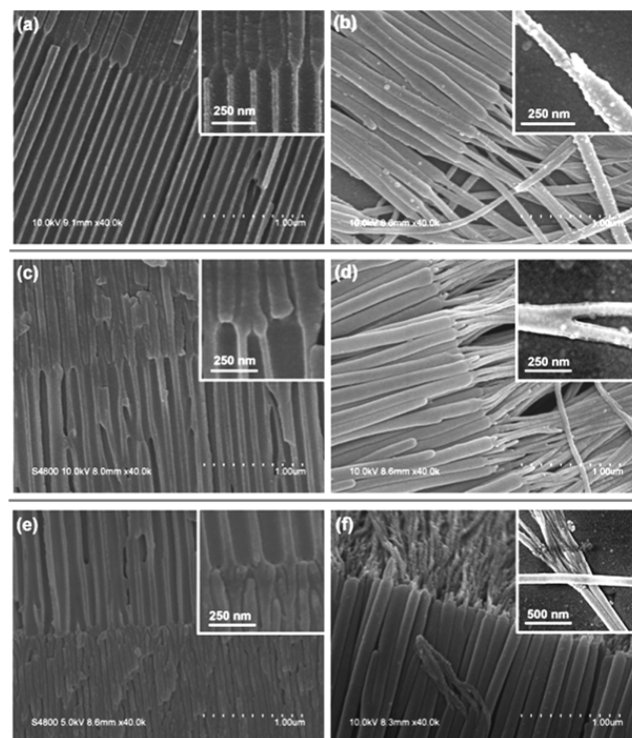


Figure 1. SEM images of the PAA membrane consisting of branching-structured nanochannels. (a) Funnel PAA membrane (nanochannel I). (c) Y-branching PAA membrane (nanochannel II). (e) Multiple branching PAA membrane (nanochannel III). The inserted images are the enlarged SEM images for each nanochannel, respectively. (b, d, f) SEM images of the CNTs fabricated in nanochannels I, II, and III, respectively.

in the middle region after template removal. Using this approach, multiple branching nanochannels (e.g., Y branching and four branches from one stem) have been fabricated.^{55–59} The SEM images in Figure 1c show the cross-section of a typical Y-branching PAA membrane (called nanochannel II) fabricated by reducing the anodizing voltage to $1/\sqrt{2} \times 60$ V. The diameter of PAA nanochannel for the top (Figure S3a, Supporting Information) and bottom (Figure S3b, Supporting Information) is about 100 and 30 nm, respectively. All the branches occur at the same depth, and the thicknesses of two-tiered layers are estimated to be ca. 45 and 30 μm (Figure S3c), respectively. The CNTs geometry (Figure 1d) fabricated from the Y branching PAA membrane is the same as the one of nanochannel II. Similarly, multiple branches (about four branches) from one stem nanochannel (Figure 1e,f and Figure S4, Supporting Information) are fabricated by reducing the anodizing voltage to $1/\sqrt{4} \times 60$ V, and the resultant membrane was named as nanochannel III. The size of the stem and branches is about 100 and 20 nm, respectively. The detailed parameters of these nanochannel arrays are listed in Table S1 (Supporting Information).

Rectification of PAA Membranes with Branching Nanochannel Array. As a kind of amphoteric material, alumina carries different surface charges upon alteration of solution pH.⁶² At solution pH lower than its isoelectric point ($pI = 6.5$), alumina will carry positive charges due to protonation. On the contrary, the alumina surface will carry negative charges due to deprotonation in solution pH above pI . As we know, ions transporting through the alumina nano-

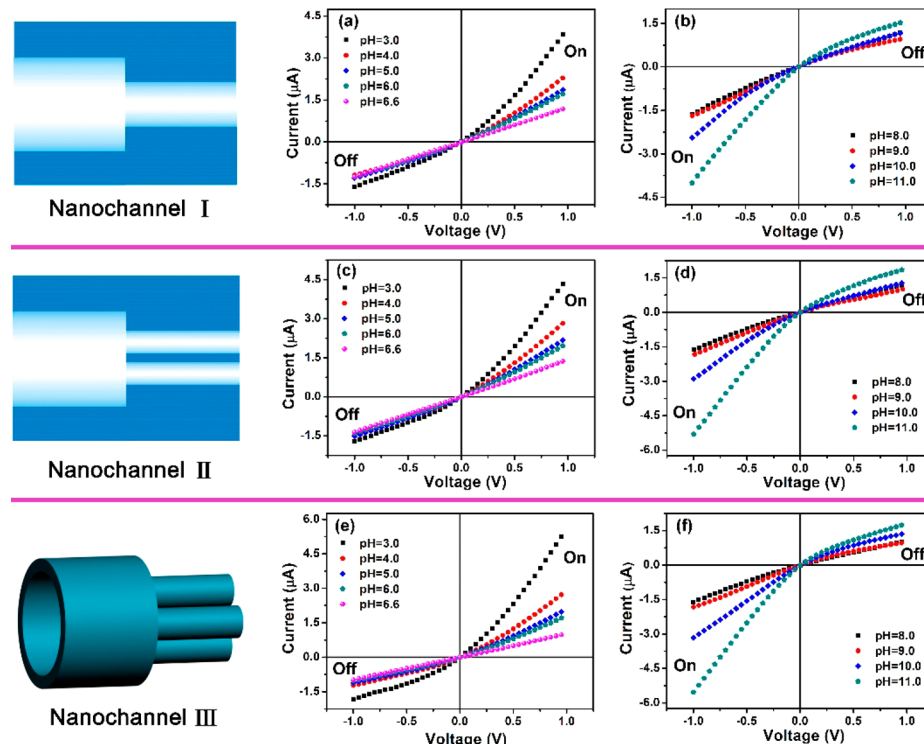


Figure 2. Experimental ionic rectification characteristics of PAA membranes consisting of different geometry nanochannels measured in 1 mM KCl with different pH values. PAA membranes were fabricated in 0.3 M oxalic acid solution. The anodization voltage for the preanodization and the first anodization were both 60 V, while the second anodization voltages were 60, 42.5, and 30 V for nanochannels I, II, and III, respectively.

channels will be modulated by the surface charges, resulting in unique transport phenomena.^{16,63,64}

The experimental setup for measuring ion transport through the branching nanochannel array is illustrated in Figure S5 and described in the Supporting Information. Figure 2a,b shows the *i*-V curves recorded using a PAA membrane consisting of nanochannel I under symmetric electrolyte conditions with different pH values of 1 mM KCl (the Debye length $\lambda \approx 10$ nm; the rectification phenomenon is not observed in the PAA channel with a higher concentration of KCl as described in Supporting Information, Figure S6).⁵ In all experiments, the working electrode is inserted in the stem side (larger size nanochannels) and the counter electrode in the branches side (smaller size nanochannels). In acidic KCl solutions, the *i*-V curves show that, as the potential applied to the working electrode is positive, the currents for positive potentials are higher than the ones for negative potentials. This observation is in accordance with the ones observed using conical nanopores carrying positive charges.^{35,37,42} At solution pH lower than the *pI* of alumina, alumina is protonated and carries positive charges. The positively charged nanochannels attract excess counterions (Cl^- and OH^-) and meanwhile exclude co-ions (K^+ and H^+) as compared to the bulk. Thus, the currents carried by anions are much larger than the ones by cations, showing the rectification characteristics of a high conducting ("on") state for $V > 0$ and a low conducting ("off") state for $V < 0$ (Figure 2a), while higher solution pH ($>\text{pI}$ of alumina) results in the deprotonation, and thus, the nanochannels carry negative charges. In this case, the reversed rectification effect of the nanochannels is observed: a high conducting ("on") state for $V < 0$ and a low conducting ("off") state for $V > 0$ (Figure 2b). These results demonstrate that the polarity of the surface charges determines the polarity of the rectification effect. It is

expected that the *i*-V curve should display a linear Ohmic feature when the net surface charges of nanochannels approach to zero, i.e., at pH = 6.6 which is close to the *pI* (6.5) of PAA fabricated in oxalic acid.²² The similar tendency of the *i*-V features for nanochannels I is also observed for the nanochannels II and III, although the ionic rectification ratio increases slightly with the increase of branching numbers, which will be discussed in the next section. In order to confirm that the observed ICR is caused by the asymmetrical geometry in our system, control experiments are carried out using a PAA membrane consisting of symmetrical nonbranching nanochannels. As shown in Figure S7, Supporting Information, all the *i*-V curves show the same linear behavior in 1 mM KCl solution with varied pH values. These results demonstrate that both the asymmetrical geometry and surface charges are essential to observe ICR in our system.

Rectification is usually represented quantitatively as the ICR ratio (r) between the currents measured at voltages of the same amplitude but opposite polarity.⁶⁵ In this work, we used the same definition as in our previous report:³¹ r is defined as the absolute value of the current ratio I (on state)/ I (off state) at ± 1 V (eq 1).

$$r = \frac{|I_{\text{on}}|}{|I_{\text{off}}|} \quad (1)$$

Figure 3 shows the variation of rectification ratio for four kinds of nanochannels as a function of solution pH. As expected, all the branching nanochannels with branching geometries show solution pH dependent ICR ratios, while the nanochannel for the control experiment with symmetric geometry does not display the ICR effect. For the branching nanochannels, their ICR ratios vary from 1 to 3 as the solution pH changes. The rectification ratio decreases with the increase

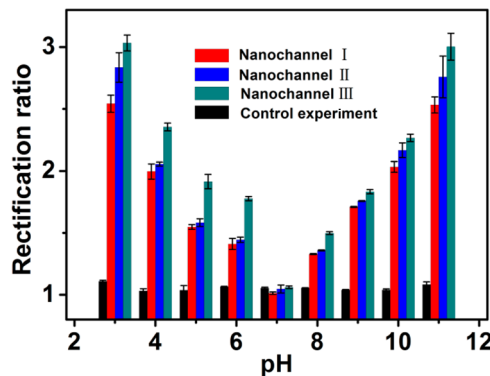


Figure 3. Ionic rectification ratio of PAA membranes consisting of different geometry nanochannels measured in 1 mM KCl with different pH values. PAA membranes were fabricated in 0.3 M oxalic acid solution. The anodization voltage for the preanodization and the first anodization were both 60 V, while the second anodization voltages were 60, 42.5, and 30 V for nanochannels I, II, and III, respectively. The control experiment was carried using PAA membrane consisting of nonbranching nanochannels, which was anodized at 60 V for both preanodization and the first anodization. Errors bars are $\pm\sigma$ for $n = 3$.

of solution pH from 3 to 7, while it increases with increasing the solution pH from 7 to 11 due to the protonation and deprotonation processes. This phenomenon clearly shows that the ICR ratio is determined by the surface charge density and charge polarity. Since the isoelectric point of PAA is close to pH 6.5, a decrease or increase of solution pH from the *pI* of

PAA will increase the surface charges due to the protonation and deprotonation processes. In addition, the rectification ratio increases slightly with the branching numbers as well, and the multiple branching (about four branches) nanochannel exhibits the highest rectification ratio over the whole solution pH range. It has been discussed above and reported previously that tip diameter is critical to ion current rectification in conical nanopores.^{25,66} In our case, the diameter of the branching nanochannels is reduced as anodization voltage decreases (Table S1, *Supporting Information*). When the primary stem is abruptly divided into four branches, the branching nanochannel diameter decreases to about 20 nm, which is the smallest among the branching nanochannels we investigated; thus, the highest rectification ratio is observed. The above experimental results reveal that the ICR ratio can be modulated by changing the solution pH and the second anodization voltage, namely, the branching numbers. Meanwhile, the rectification polarity can be reversed at solution pH approaching to *pI* of alumina as reference.

Numerical Simulation for Ionic Transport in PAA Membranes with Branching Nanochannel Array. The detailed information for the numerical simulation is described in the *Supporting Information*, including numerical equations and boundary conditions. As shown in Figure 4, the current–voltage (*i*–*V*) profiles of a single nanochannel are simulated at voltage bias from −1 to +1 V. To clarify the influence of surface charges on the rectification effect, we measured the conductance of KCl electrolyte (pH 6.6) as a function of concentration (Figure S11, *Supporting Information*) and calculated the surface charge density to be $\sigma = -0.5 \text{ mC/m}^2$

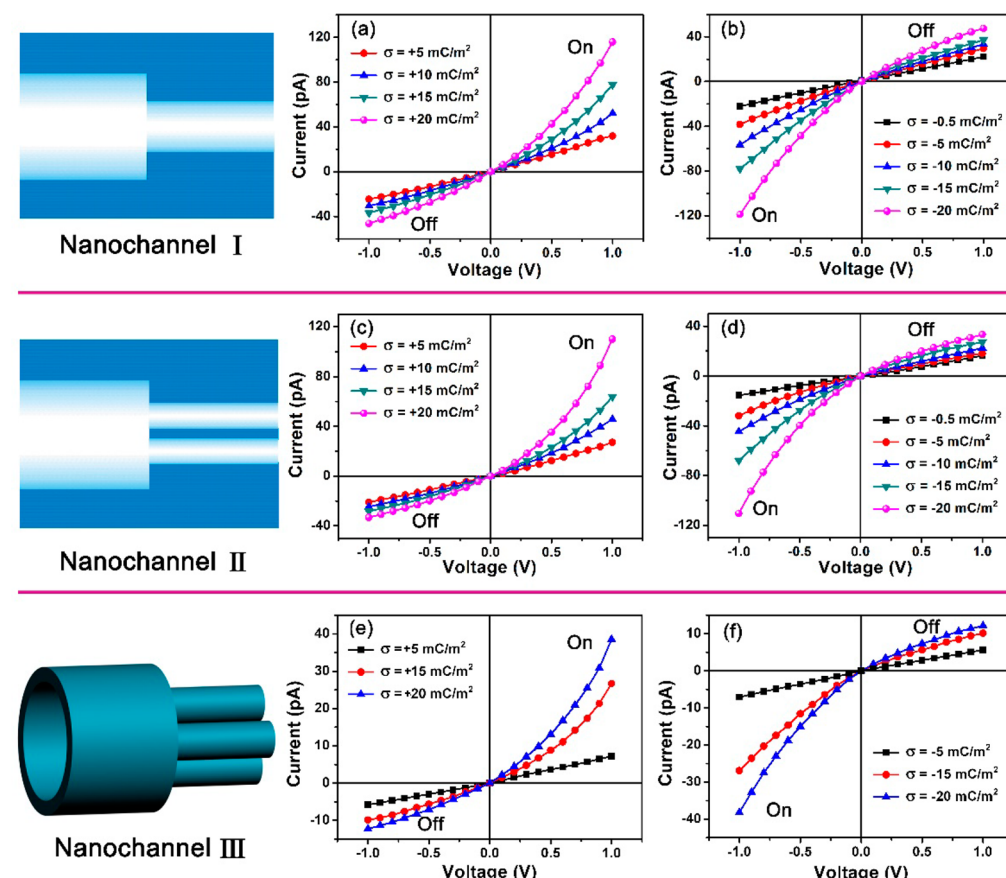


Figure 4. Simulated *i*–*V* profiles of different nanochannels with different sizes and surface charge densities.

(refers to Supporting Information).⁶⁷ The simulation results show a linear i - V relationship in the three asymmetrical nanochannels (Figure 4b,d, black curves). These phenomena demonstrate that the asymmetric geometry alone cannot result in ICR and the surface charge σ is essential to induce the rectification effect. As the surface charge density σ increases, the ICR effect occurs, resulting in an increase of rectification ratio (Figure 5). These results are in good agreement with the

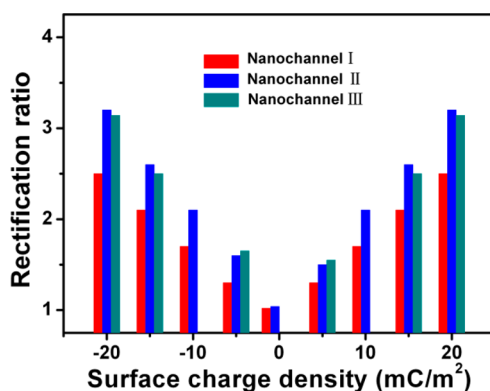


Figure 5. Simulated ionic rectification ratios of different nanochannels with different sizes and surface charge densities.

simulated results for asymmetric nanopores.⁶⁸ The rectification ratio depends critically on surface charge density for all asymmetric geometry nanochannels in our experiments, and all simulated i - V curves show the same qualitative behavior.

The ion accumulation and depletion models can be used to qualitatively explain the ICR as previously reported.^{69–73} Since the ICR can be ascribed to the variation of ion concentration in the nanochannel due to the static electric potential and electric migration. The changes of the potential are analyzed (Figure 6).

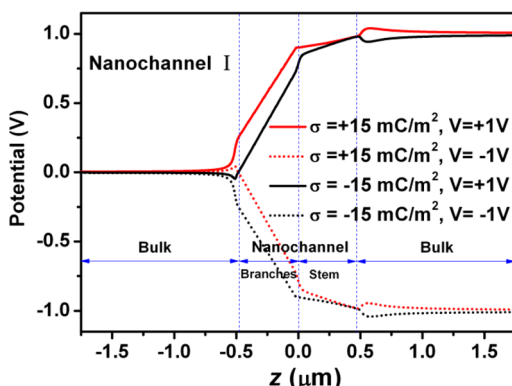


Figure 6. Potential distributions calculated along the symmetry axis of nanochannel I with opposite polarity charge ($\sigma_1 = +15 \text{ mC}/\text{m}^2$, $\sigma_2 = -15 \text{ mC}/\text{m}^2$).

It is clear that the electric potential profiles are strongly nonlinear in the branching nanochannel region regardless of the surface charge polarities. The electric potential mainly drops in the branching nanochannels, accounting for 3/4 of the total applied potential, while there is only about 1/4 potential drop in the stem nanochannel. These results signify the importance of surface charges and also demonstrate that the electric potential at the geometry transitional area will effectively influence the ion concentrations in this region.

Ionic Concentration Profiles in PAA Membranes with Branching Nanochannel Array. We highlight various similarities and differences of ionic concentration distribution in nanochannels responding to external applied voltage between nanochannel I and nanochannel II. Both the concentrations of K^+ and Cl^- are normalized by the bulk concentration (1 mM KCl). The lengths of the models are normalized by the total length of the model (4 μm). Figure 7 shows the distribution of ionic concentrations along the centerline of the y direction of the nanochannel for nanochannels I and II (Figures S8a and S9, Supporting Information). The effect of funnel geometry in the nanochannel is investigated in the Supporting Information (Figure S8b,c). As shown in Figure 7a, when a +1 V electric field is applied from the stem (gray region) to branching (dark yellow region) nanochannel, both the concentrations of K^+ (red solid line) and Cl^- (black solid line) ions increase in the whole nanochannel and accumulate even more in the branch nanochannel (dark yellow region). The accumulated ions result in the increase of ion conductance of the nanochannel. When a -1 V bias is applied, both the concentrations of K^+ and Cl^- ions are lower in the stem and branching channels than those of +1 V bias; however, they are still significantly higher than the bulk concentration. Since the nanochannel carries positive surface charges, the strong electrostatic interactions will attract more negatively charged Cl^- ions into the branching nanochannel than into the stem channel due to the size difference of nanochannels, resulting in accumulation of Cl^- ions in the branching nanochannel even at a -1 V bias. However, it is difficult for K^+ ions to enter the whole nanochannel due to the strong electrostatic repulsion. The formation of ions depletion and enrichment zones in the nanochannel results in ionic current variations at open state (+1 V) and close state (-1 V). The concentration difference between counterions and co-ions in the nanochannel is about 1, which is used to neutralize the positive surface charges of the nanochannel.

In the case of nanochannel II, an enlarged ion concentration polarization (ICP) is observed in ionic distribution (Figure 7b) outside of the nanochannel. For clarity, we analyze the profile of ionic concentrations in one of the branch channels connecting to the stem nanochannel. As shown in Figure 7b, when nanochannel II is at an open state (1 V bias), the normalized concentrations of K^+ (red solid line) and Cl^- (black solid line) are significantly higher than their bulk concentrations. They increase rapidly to the maximum values of 6.5 and 7.5, respectively, at the interface between branch (dark yellow region) and stem nanochannels (gray region). When the nanochannel is at a closed state (-1 V), both the K^+ (red dashed line) and Cl^- (black dashed line) concentrations in the branch nanochannel are higher than the bulk although they are only ca. half of the concentrations in the open state. However, they reach the maximum profiles at the inlet of the branch nanochannel and decrease rapidly along the nanochannel to ca. bulk values at the interface. They decrease again rapidly in the stem nanochannel and reach almost zero, forming a depletion region in the stem nanochannel. However, due to the propagation of ICP, enlarged enrichment and depletion regions are observed at both outer sides of the nanochannel II. As illustrated in Figure 8e–h, we observe the stronger ICP near the junctions between nanochannel II and the reservoirs than those of nanochannel I (Figure 8a–d). Since the color scale has difficulty in clearly displaying the large difference of concentration in the nanochannel, we adopt a logarithmic

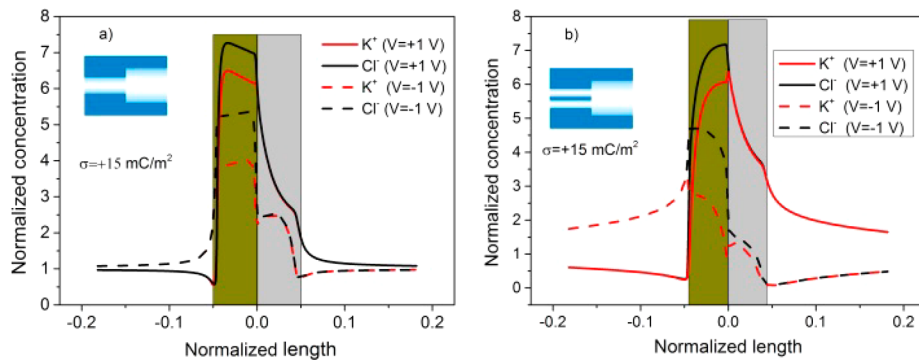


Figure 7. Comparison of the distribution of KCl along the centerline of the axial direction for the different structures of the nanochannels with a positive surface charge ($+15 \text{ mC/m}^2$). Ionic concentration distribution in nanochannels I (a) and II (b). Red and black lines represent the concentration distributions of K⁺ and Cl⁻ at voltage bias (+1 V, solid line; -1 V, dashed line), respectively. Both the concentrations of K⁺ and Cl⁻ were normalized by the bulk concentration (1 mM KCl). The lengths of the models were normalized by the total length of the model (4 μm).

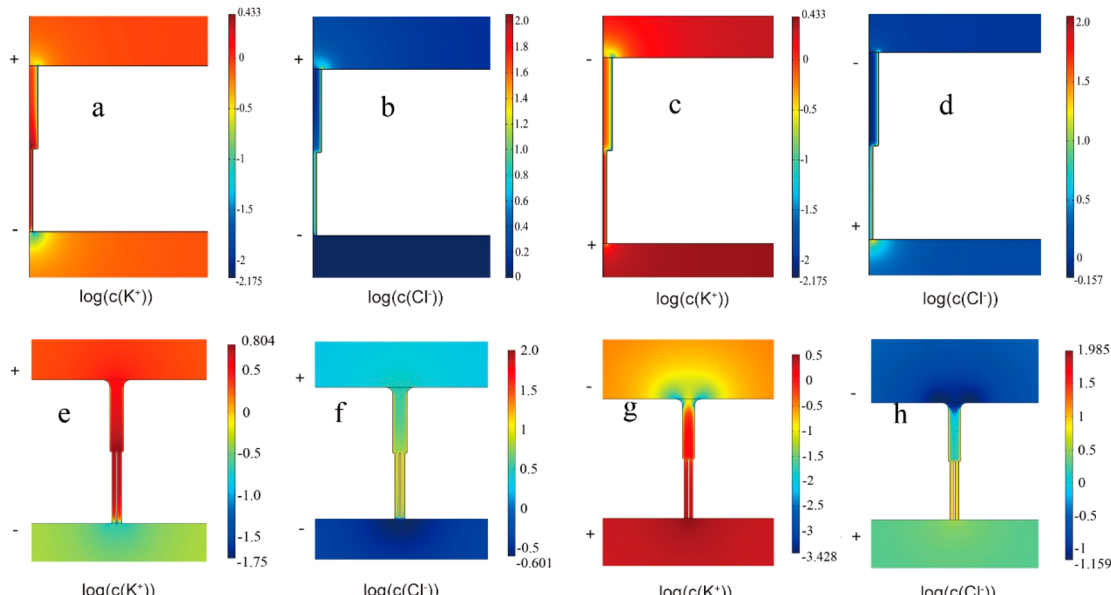


Figure 8. Numerical results of KCl concentration distribution (logarithmic scale in concentration) in positively charged nanochannel I and nanochannel II ($\sigma = +15 \text{ mC/m}^2$) with different voltage bias. (a-d) represent the concentration profiles of K⁺ and Cl⁻ ions at $\pm 1 \text{ V}$ bias in nanochannel I, respectively; (e-h) represent the concentration profiles of K⁺ and Cl⁻ ions at $\pm 1 \text{ V}$ bias, respectively. The + and - signs refer to the polarity of the voltage applied across the nanochannel.

scale in the concentration profile. Figure S12, *Supporting Information*, shows the concentration profile in nanochannels I and II ($\sigma = +15 \text{ mC/m}^2$). The concentration profiles in negatively charged nanochannels I and II ($\sigma = -15 \text{ mC/m}^2$) are described in Figures S13–14, *Supporting Information*. The existence of enlarged ICP results in the establishment of a potential of concentration differences across the nanochannel, which counterbalances the external applied potential and thus decreases the electric field of the nanochannel. Therefore, the observed currents and ICR values for nanochannel II do not increase significantly as compared to the nanochannel I.

Recently, Santiago and co-workers⁷⁴ studied the propagation of ICP at the interface between nanochannel and microchannel. They classified the ICP into two states: ICP with and without propagation. Tallareket and co-workers⁷⁵ investigated the propagation of ICP in asymmetric nanochannels with serial connection and found that enriched ICP was developed into adjoining channel, while the depleted ICP remained stationary. They attributed the propagation of ICP to the interaction of

nanochannel Dukhin number and mobility of co-ions non-dimensionalized by the electroosmotic mobility. The following equations (eqs 2–3) have been used to predict the propagation of ICP zone in nanochannels.^{74,75}

$$c \frac{Fd}{\sigma} < \max(\nu, 2\nu - 1) \quad (2)$$

where ν is the dimensionless mobility of the co-ions, defined as

$$\nu = -\frac{u_{\text{ep}}}{u_{\text{eof}}} \quad (3)$$

where d is the diameter of the nanochannel, u_{ep} is the electrophoretic velocity of co-ions, and u_{eof} is the electroosmotic velocity in the nanochannel. When eq 2 is satisfied, the ICP zone will extend over a larger distance from the nanochannel to the reservoir. Otherwise, the ICP zone maintains stationary and is localized in the nanochannel.

Similarly, we use this method to evaluate the propagation of ICP in nanochannel II. First, we compared the values of two

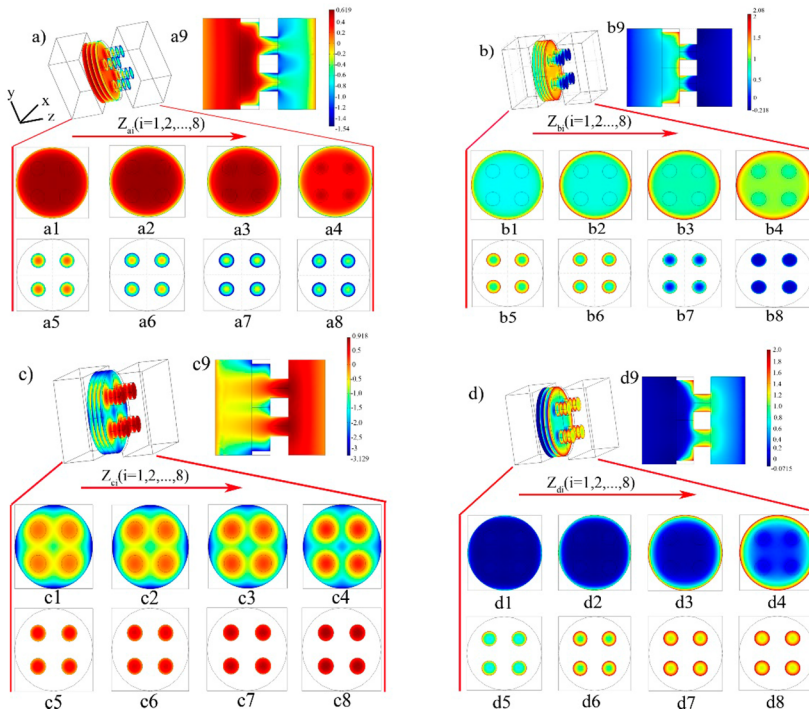


Figure 9. Ionic concentrations profiles (logarithmic scale in concentration) calculated using a 3D numerical simulation for nanochannel III with surface charge $\sigma = +15 \text{ mC/m}^2$. Stem nanochannel: 50 nm in length and 100 nm in diameter; branching nanochannels: 50 nm in length and 20 nm in diameter. The x - y cross-sectional concentration images of K^+ (a, c1–8) and Cl^- ions (b, d1–8) in nanochannels are taken at 10, 20, 30, 40, 60, 72, 84, and 96 nm along the z axis. a–d9 display the cross-sectional concentration images of K^+ and Cl^- ions in the y - z plane, respectively. Voltage bias: +1 V (a and b); -1 V (c and d).

sides of eq 2 in our system. As defined in eq 2, we know that the left-hand side of equation (the inverse Dukhin number) is determined by the physicochemical characteristics of the nanochannel and system (surface charge, diameter of nanochannel, and concentration of bulk electrolyte), while the right-hand side of this equation is dominated by the mass transport in the nanochannel. The diameter of branch and stem nanochannels are 20 and 100 nm, respectively. The surface charge densities of both nanochannels are $+15 \text{ mC/m}^2$. The bulk concentration of electrolyte is 1 mM. The calculated inverse Dukhin numbers are 1.287×10^{-4} and 6.433×10^{-4} for branch nanochannel and stem nanochannel, respectively. Then, we apply the calculated average electroosmotic velocity and the electrophoretic velocity (calculation refers to Figure S15 in Supporting Information) into eq 3 and calculate the right-hand side of eq 2. The dimensionless motilities of co-ions (K^+ ions) are 0.159 and 0.2 for branch and stem nanochannels, respectively. Therefore, for eq 2, the maximum values of the right-hand side for both the branch and stem nanochannels are always larger than the ones for the left-hand side. The ICP zones will thus propagate outward the nanochannels to reservoirs.

In the case of nanochannel III with multiple branches, a 2D model cannot exactly reflect the real geometry. Thus, a 3D model is built for the case of nanochannel III (Figure S10, Supporting Information). The current–voltage (i – V) characteristics (Figure 4e,f) of multiple nanochannels are simulated at varied voltage bias ranging from -1 to +1 V. The rectification direction is related to the polarity of surface charges, which are in accordance with the results for nanochannels I and II. The simulated rectification ratio (Figure 5) is closely related to the surface charge density, which is in good agreement with the

experimental values. Figure 9 shows the detailed ionic distribution profiles (for clarity, concentration is plotted in logarithmic scale) in nanochannel III with surface charge density of $\sigma = +15 \text{ mC/m}^2$ for different voltages obtained from our numerical simulation. Since the nanochannel surface carries positive charges, the ionic concentrations (Figure 9a,c) of K^+ in whole nanochannels are lower than Cl^- ions (Figure 9b,d) at $\pm 1 \text{ V}$ bias due to the stronger electrostatic repulsion. At +1 V bias, K^+ ions concentration in nanochannel III gradually decreases from the stem nanochannel to branching nanochannel (Figure 9a9) since the electrostatic repulsion force rapidly increases in the branching nanochannel due to the smaller size. Similar trends in concentration distribution for Cl^- ions are also observed. Thus, the nanochannel III displays enlarged ICP regions for both ions. Detailed concentration distributions of both anions and cations can be analyzed by the x - y cross-sectional images at different positions of the nanochannel. It is observed that K^+ ions are concentrated near the center of the nanochannel (Figure 9a1–a4) and branching nanochannels (Figure 9a5–a8) due to the electrostatic repulsion, while Cl^- ions are accumulated near surfaces of the nanochannel (Figure 9b1–b4) and branching nanochannels (Figure 9b5–b8) for equilibrating the positive surface charges. Interestingly, the concentration profiles for both ions in the stem nanochannel are strongly influenced by the branching nanochannels. This phenomenon becomes more significant as the cross-sectional plane approaches the junction interface. Near the junction interface, four accumulation regions for both ions appear in the stem nanochannel corresponding to the positions of branching nanochannels, respectively. When the applied voltage bias is changed to -1 V, the concentration profiles of K^+ and Cl^- gradually decrease from the branching

nanochannels to the stem nanochannel (Figure 9c9,d9) due to the directional migration of K^+ (from stem to branching nanochannel) and Cl^- (from branching nanochannels to stem nanochannel). Enlarged ICP regions for both ions are also observed. The distribution trends for both ions at different positions of nanochannels are similar as in the case of +1 V, although their concentrations in nanochannels at -1 V are lower than the ones at +1 V. However, the influence of branching nanochannels on the concentration profiles of both ions in the stem nanochannel becomes much larger at -1 V as compared to the ones at +1 V. Our 3D simulation results demonstrate that nonuniform distributions of K^+ and Cl^- ions in the stem nanochannel occur significantly due to the presence of branching nanochannels, especially near the junction interface. When the surface charge density is changed to -15 mC/m², the ion concentrations (Figure S16, Supporting Information) are similar to the ones at $\sigma = +15 \text{ mC/m}^2$. The main difference is that the major current carrier is K^+ instead of Cl^- ions.

CONCLUSIONS

In conclusion, we demonstrate that pH-dependent ionic current rectification can be achieved using a porous anodic alumina membrane with a tailor-made branching nanochannels array. The experimental results demonstrate that the rectification polarity and rectification ratio can be accomplished within the same device simply by varying solution pH, which closely mimics the gating mechanism of biological channels. In addition, we report the study of ion rectification using a 3D model for reflecting the nature of ions transport in branching nanochannels. Simulation results show that ICR is mainly caused by ions accumulation and depletion in nanochannels regulated by the size of branching nanochannels and the surface charge density. In addition, 3D simulations can give more detailed information on concentration profiles in the stem-branching system, i.e., existence of nonuniform ionic distributions in stem nanochannel due to the presence of branching nanochannels. The results would promote our understanding of the mechanism of hybrid nanochannel rectification and extend its application.

ASSOCIATED CONTENT

Supporting Information

Detailed information for experimental and theoretical section and additional SEM images. The Supporting Information is available free of charge on the ACS Publications website at DOI: 10.1021/acs.analchem.5b01016.

AUTHOR INFORMATION

Corresponding Author

*E-mail: xhxia@nju.edu.cn. Fax: (+86)-25-83685947.

Author Contributions

[‡]C.-Y.Li and Z.-Q.Wu contributed equally.

Notes

The authors declare no competing financial interest.

ACKNOWLEDGMENTS

This work was supported by the Grants from the National 973 Basic Research Program (2012CB933800) and the National Natural Science Foundation of China (21275070, 21275071, 21327902, 21405024). We also gratefully acknowledge the

HPCC (High-Performance Computing Center) of Nanjing University.

REFERENCES

- (1) Hummer, G.; Rasaiah, J. C.; Noworyta, J. P. *Nature* **2001**, *414*, 188–190.
- (2) Duan, C.; Majumdar, A. *Nat. Nanotechnol.* **2010**, *5*, 848–852.
- (3) Tsukahara, T.; Hibara, A.; Ikeda, Y.; Kitamori, T. *Angew. Chem., Int. Ed.* **2007**, *46*, 1180–1183.
- (4) Chinen, H.; Mawatari, K.; Pihosh, Y.; Morikawa, K.; Kazoe, Y.; Tsukahara, T.; Kitamori, T. *Angew. Chem., Int. Ed.* **2012**, *51*, 3573–3577.
- (5) Chen, W.; Wu, Z. Q.; Xia, X. H.; Xu, J. J.; Chen, H. Y. *Angew. Chem., Int. Ed.* **2010**, *49*, 7943–7947.
- (6) Hornblower, B.; Coombs, A.; Whitaker, R. D.; Kolomeisky, A.; Picone, S. J.; Meller, A.; Akeson, M. *Nat. Methods* **2007**, *4*, 315–317.
- (7) Jirage, K. B.; Hulteen, J. C.; Martin, C. R. *Science* **1997**, *278*, 655–658.
- (8) Lakshmi, B. B.; Martin, C. R. *Nature* **1997**, *388*, 758–760.
- (9) Lee, S. B.; Mitchell, D. T.; Trofin, L.; Nevanen, T. K.; Söderlund, H.; Martin, C. R. *Science* **2002**, *296*, 2198–2200.
- (10) Striemer, C. C.; Gaborski, T. R.; McGrath, J. L.; Fauchet, P. M. *Nature* **2007**, *445*, 749–753.
- (11) Kim, S. J.; Ko, S. H.; Kang, K. H.; Han, J. *Nat. Nanotechnol.* **2010**, *5*, 297–301.
- (12) Majumder, M.; Chopra, N.; Andrews, R.; Hinds, B. J. *Nature* **2005**, *438*, 44–44.
- (13) Wu, J.; Gerstandt, K.; Zhang, H.; Liu, J.; Hinds, B. J. *Nat. Nanotechnol.* **2012**, *7*, 133–139.
- (14) Vlassiouk, I.; Kozel, T. R.; Siwy, Z. S. *J. Am. Chem. Soc.* **2009**, *131*, 8211–8220.
- (15) Ali, M.; Neumann, R.; Ensinger, W. *ACS Nano* **2010**, *4*, 7267–7274.
- (16) Li, S. J.; Li, J.; Wang, K.; Wang, C.; Xu, J. J.; Chen, H. Y.; Xia, X. H.; Huo, Q. *ACS Nano* **2010**, *4*, 6417–6424.
- (17) Ali, M.; Tahir, M. N.; Siwy, Z.; Neumann, R.; Tremel, W.; Ensinger, W. *Anal. Chem.* **2011**, *83*, 1673–1680.
- (18) Zhou, K.; Li, L.; Tan, Z.; Zlotnick, A.; Jacobson, S. C. *J. Am. Chem. Soc.* **2011**, *133*, 1618–1621.
- (19) Kohli, P.; Harrell, C. C.; Cao, Z.; Gasparac, R.; Tan, W.; Martin, C. R. *Science* **2004**, *305*, 984–986.
- (20) Venkatesan, B. M.; Bashir, R. *Nat. Nanotechnol.* **2011**, *6*, 615–624.
- (21) Siwy, Z.; Trofin, L.; Kohli, P.; Baker, L. A.; Trautmann, C.; Martin, C. R. *J. Am. Chem. Soc.* **2005**, *127*, 5000–5001.
- (22) Miao, J. Y.; Xu, Z. L.; Zhang, X. Y.; Wang, N.; Yang, Z. Y.; Sheng, P. *Adv. Mater.* **2007**, *19*, 4234–4237.
- (23) Guo, W.; Cao, L.; Xia, J.; Nie, F. Q.; Ma, W.; Xue, J.; Song, Y.; Zhu, D.; Wang, Y.; Jiang, L. *Adv. Funct. Mater.* **2010**, *20*, 1339–1344.
- (24) Wen, L.; Hou, X.; Tian, Y.; Nie, F. Q.; Song, Y.; Zhai, J.; Jiang, L. *Adv. Mater.* **2010**, *22*, 1021–1024.
- (25) Kovarik, M. L.; Zhou, K.; Jacobson, S. C. *J. Phys. Chem. B* **2009**, *113*, 15960–15966.
- (26) Wei, C.; Bard, A. J.; Feldberg, S. W. *Anal. Chem.* **1997**, *69*, 4627–4633.
- (27) Karnik, R.; Duan, C.; Castelino, K.; Daiguji, H.; Majumdar, A. *Nano Lett.* **2007**, *7*, 547–551.
- (28) Yan, R.; Liang, W.; Fan, R.; Yang, P. *Nano Lett.* **2009**, *9*, 3820–3825.
- (29) Cheng, L. J.; Guo, L. J. *Nano Lett.* **2007**, *7*, 3165–3171.
- (30) Cheng, L. J.; Guo, L. J. *ACS Nano* **2009**, *3*, 575–584.
- (31) Li, C. Y.; Ma, F. X.; Wu, Z. Q.; Gao, H. L.; Shao, W. T.; Wang, K.; Xia, X. H. *Adv. Funct. Mater.* **2013**, *23*, 3836–3844.
- (32) Siwy, Z.; Heins, E.; Harrell, C. C.; Kohli, P.; Martin, C. R. *J. Am. Chem. Soc.* **2004**, *126*, 10850–10851.
- (33) Umehara, S.; Pourmand, N.; Webb, C. D.; Davis, R. W.; Yasuda, K.; Karhanek, M. *Nano Lett.* **2006**, *6*, 2486–2492.
- (34) Vlassiouk, I.; Siwy, Z. S. *Nano Lett.* **2007**, *7*, 552–556.

- (35) Ali, M.; Ramirez, P.; Mafé, S.; Neumann, R.; Ensinger, W. *ACS Nano* **2009**, *3*, 603–608.
- (36) Davenport, M.; Rodriguez, A.; Shea, K. J.; Siwy, Z. S. *Nano Lett.* **2009**, *9*, 2125–2128.
- (37) Yameen, B.; Ali, M.; Neumann, R.; Ensinger, W.; Knoll, W.; Azzaroni, O. *J. Am. Chem. Soc.* **2009**, *131*, 2070–2071.
- (38) Zhang, L. X.; Cao, X. H.; Zheng, Y. B.; Li, Y. Q. *Electrochim. Commun.* **2010**, *12*, 1249–1252.
- (39) Lan, W. J.; Holden, D. A.; White, H. S. *J. Am. Chem. Soc.* **2011**, *133*, 13300–13303.
- (40) Sa, N.; Baker, L. A. *J. Am. Chem. Soc.* **2011**, *133*, 10398–10401.
- (41) Zhang, L. X.; Cai, S. L.; Zheng, Y. B.; Cao, X. H.; Li, Y. Q. *Adv. Funct. Mater.* **2011**, *21*, 2103–2107.
- (42) Zhang, M.; Hou, X.; Wang, J.; Tian, Y.; Fan, X.; Zhai, J.; Jiang, L. *Adv. Mater.* **2012**, *24*, 2424–2428.
- (43) Kalman, E. B.; Vlassiuk, I.; Siwy, Z. S. *Adv. Mater.* **2008**, *20*, 293–297.
- (44) Ali, M.; Ramirez, P.; Nguyen, H. Q.; Nasir, S.; Cervera, J.; Mafe, S.; Ensinger, W. *ACS Nano* **2012**, *6*, 3631–3640.
- (45) Zhang, Q. Q.; Hu, Z. Y.; Liu, Z. Y.; Zhai, J.; Jiang, L. *Adv. Funct. Mater.* **2014**, *24*, 424–431.
- (46) Wang, H. M.; Hou, S. N.; Wang, Q. Q.; Wang, Z. W.; Xia, F.; Zhai, J. *J. Mater. Chem. B* **2015**, *3*, 1699–1705.
- (47) Zhang, Q. Q.; Liu, Z. Y.; Wang, K. F.; Zhai, J. *Adv. Funct. Mater.* **2015**, *25*, 2091–2098.
- (48) Kong, Y.; Xia, F.; Zhang, M. H.; Hou, X.; Liu, Z. Y.; Zhai, J.; Jiang, L. *ACS Appl. Mater. Interfaces* **2013**, *5*, 7931–7936.
- (49) Li, J.; Stein, D.; McMullan, C.; Branton, D.; Aziz, M. J.; Golovchenko, J. A. *Nature* **2001**, *412*, 166–169.
- (50) Ali, M.; et al. *Nanotechnology* **2008**, *19*, 085713.
- (51) Storm, A. J.; Chen, J. H.; Ling, X. S.; Zandbergen, H. W.; Dekker, C. *Nat. Mater.* **2003**, *2*, 537–540.
- (52) Kowalczyk, S. W.; Kapinos, L.; Blosser, T. R.; Magalhaes, T.; van Nies, P.; LimRoderick, Y. H.; Dekker, C. *Nat. Nanotechnol.* **2011**, *6*, 433–438.
- (53) Liu, S.; Dong, Y.; Zhao, W.; Xie, X.; Ji, T.; Yin, X.; Liu, Y.; Liang, Z.; Momotenko, D.; Liang, D.; Girault, H. H.; Shao, Y. *Anal. Chem.* **2012**, *84*, 5565–5573.
- (54) Masuda, H.; Fukuda, K. *Science* **1995**, *268*, 1466–1468.
- (55) Meng, G.; Jung, Y. J.; Cao, A.; Vajtai, R.; Ajayan, P. M. *Proc. Natl. Acad. Sci. U. S. A.* **2005**, *102*, 7074–7078.
- (56) Meng, G.; Han, F.; Zhao, X.; Chen, B.; Yang, D.; Liu, J.; Xu, Q.; Kong, M.; Zhu, X.; Jung, Y. J.; Yang, Y.; Chu, Z.; Ye, M.; Kar, S.; Vajtai, R.; Ajayan, P. M. *Angew. Chem.* **2009**, *121*, 7302–7306.
- (57) Chen, B.; Meng, G.; Xu, Q.; Zhu, X.; Kong, M.; Chu, Z.; Han, F.; Zhang, Z. *ACS Nano* **2010**, *4*, 7105–7112.
- (58) Han, F.; Meng, G.; Xu, Q.; Zhu, X.; Zhao, X.; Chen, B.; Li, X.; Yang, D.; Chu, Z.; Kong, M. *Angew. Chem., Int. Ed.* **2011**, *50*, 2036–2040.
- (59) Li, X.; Meng, G.; Xu, Q.; Kong, M.; Zhu, X.; Chu, Z.; Li, A. P. *Nano Lett.* **2011**, *11*, 1704–1709.
- (60) Miao, J. Y.; Cai, Y.; Chan, Y. F.; Sheng, P.; Wang, N. *J. Phys. Chem. B* **2006**, *110*, 2080–2083.
- (61) Li, J.; Papadopoulos, C.; Xu, J. *Nature* **1999**, *402*, 253–254.
- (62) Chen, W.; Yuan, J. H.; Xia, X. H. *Anal. Chem.* **2005**, *77*, 8102–8108.
- (63) Gao, H. L.; Zhou, K. L.; Wang, C.; Li, S. J.; Zhang, H.; Xia, X. H. *Electrochemistry* **2012**, *18*, 229–234.
- (64) Gao, H. L.; Zhang, H.; Li, C. Y.; Xia, X. H. *Electrochim. Acta* **2013**, *110*, 159–163.
- (65) Harrell, C. C.; Kohli, P.; Siwy, Z.; Martin, C. R. *J. Am. Chem. Soc.* **2004**, *126*, 15646–15647.
- (66) Singh, K. P.; Kumar, M. *J. Phys. Chem. C* **2011**, *115*, 22917–22924.
- (67) Schoch, R. B.; Renaud, P. *Appl. Phys. Lett.* **2005**, *86*, 253111.
- (68) Momotenko, D.; Cortes-Salazar, F.; Josserand, J.; Liu, S.; Shao, Y.; Girault, H. H. *Phys. Chem. Chem. Phys.* **2011**, *13*, 5430–5440.
- (69) Daiguji, H. *Chem. Soc. Rev.* **2010**, *39*, 901–911.
- (70) Schoch, R. B.; Han, J.; Renaud, P. *Rev. Mod. Phys.* **2008**, *80*, 839–883.
- (71) Cheng, L. J.; Guo, L. J. *Chem. Soc. Rev.* **2010**, *39*, 923–938.
- (72) Siwy, Z. S.; Howorka, S. *Chem. Soc. Rev.* **2010**, *39*, 1115–1132.
- (73) Wang, C.; Xu, J. J.; Chen, H. Y.; Xia, X. H. *Sci. China: Chem.* **2012**, *55*, 453–468.
- (74) Zangle, T. A.; Mani, A.; Santiago, J. G. *Chem. Soc. Rev.* **2010**, *39*, 1014–1035.
- (75) Hlushkou, D.; Perry, J. M.; Jacobson, S. C.; Tallarek, U. *Anal. Chem.* **2012**, *84*, 267–274.